Mon. Not. R. Astron. Soc. **315**, 722–734 (2000)

Synthetic line profiles of rotationally distorted hot-star winds

Tim J. Harries★
Department of Physics and Astronomy, University College London, Gower Street, London WC1E 6BT

Accepted 2000 February 3. Received 2000 January 27; in original form 1999 October 20

ABSTRACT

A new Monte Carlo stellar wind radiative-transfer code is presented. The code employs a three-dimensional opacity grid, and fully treats polarization and multiple scattering. Either Mie or Rayleigh scattering phase matrices may be used, and the line-transfer is treated by means of the Sobolev approximation. Variance reduction techniques are employed to increase computational efficiency.

The results of several tests of the code are reported. It is confirmed that no continuum polarization is produced in the spherically symmetric wind case, and that the line profiles computed match those computed using established radiative-transfer codes. The continuum polarization produced by a latitudinally structured low-density wind is found to be in good agreement with that predicted by the single-scattering analytical treatment of Fox, while in the higher density regime the polarizations are consistent with the multiple-scattering code given by Hillier.

Two illustrative applications of the code are described, using the wind parameters of ζ Puppis [O4 I(n)f] as the base model. In the first the effect on the line profile of a corotating spiral density enhancement is examined. It is found that the spiral gives line profile variations on the order of 5 per cent, and that it produces an S-wave-like pattern as a function of rotational phase. It is noted that the accelerations described by the spiral wave may mimic those produced by tangentially accelerating wind clumps. The variable polarization produced by the spiral is found to have an amplitude of 0.1 per cent, with two maxima per rotational period in phase with the line emission modulation. The second application investigates the profiles and polarization produced in a clumped wind. Although the parameters of the discrete wind clumps are necessarily arbitrary, it is found that a clumped-wind model reproduces the level of spectroscopic variability found by Eversberg et al. It is shown that the wind emission 'bumps' produced in the synthetic spectra often arise from the superposition in velocity space of flux from several spatially discrete wind blobs. Although the two example models may, in combination, reproduce the observed spectroscopic variability of OB supergiants, it appears that the predicted polarimetric variability of these models is too weak to explain the polarimetric observations of OB stars by Hayes and Lupie & Nordsieck.

Finally, a new line polarization effect is described, resulting from line absorption of continuum photons in a rotating wind. The effect has a striking resemblance to the observations of ζ Puppis presented by Harries & Howarth (1996), and it is possible that the Hα polarization structure observed arises from this effect, rather than by line dilution of a continuum polarization.

Key words: polarization – radiative transfer – stars: early-type – stars: mass-loss – stars: rotation.

1 INTRODUCTION

Early-type stars lose mass via high-density, supersonic stellar winds that are driven by radiation pressure on spectral lines. Although radiation-hydrodynamic models are capable of reproducing the broad characteristics of the outflows (e.g. Friend & Abbott 1986; Howarth & Prinja 1989), it is becoming apparent that stellar rotation may play an important role in modifying the wind dynamics and hence the radiative transfer.

Observational evidence for rotational modulation of stellar

★ E-mail: th@star.ucl.ac.uk

© 2000 RAS

wind variability is difficult to gather because, although the stars are often rapidly rotating, with $v_{\rm rot} \sin i > 200\,{\rm km\,s^{-1}}$ (Howarth et al. 1997), the typical stellar radii of $\sim 20\,{\rm R}_\odot$ of OB supergiants mean that rotational periods are often on the order of a few days. Stochastic variability (perhaps produced by line-driven instabilities) frequently complicates the situation, and it may be necessary to observe several rotation periods before the rotational modulation of the wind is clearly identifible (e.g. Massa et al. 1995). Despite these problems, recent studies using intensively sampled spectroscopic time-series have found evidence for rotational modulation of the winds of early-type stars such as ζ Puppis (Howarth, Prinja & Massa 1995; Reid & Howarth 1996) and HD 64760 (Fullerton et al. 1997).

Rapid rotation may affect the stellar wind in two ways. The first is by the production of a global latitudinal dependence of the wind speed and mass-loss rate. The incorporation of centrifugal terms into 1D radiatively driven wind theory leads to the prediction that a rotating star will have the largest mass-loss at the equator (where the effective surface gravity is lowest) and the largest terminal velocity at the poles (since the terminal velocity is proportional to the surface gravity). For the highest rotation rates (when the star is rotating close to its break-up speed) wind compression may be a factor, with wind streamlines from the upper and lower hemispheres colliding at the equator and forming a disc (Bjorkmann & Cassinelli 1993). However, detailed radiation-hydrodynamics models have shown that the inclusion of non-radial azimuthal line-driving terms may impede disc formation, and that gravity darkening may in fact lead to a rarified equatorial wind (Owocki, Cranmer & Gayley 1996).

The second effect of rotation on stellar-wind morphology arises if the mass-loss rate per unit area of stellar surface is non-uniform, perhaps due to the presence of star spots or a corotating magnetic field. In this case, radial streams of higher density material are twisted into spiral structures bounded by shocks (Cranmer & Owocki 1996). These corotating interaction region (CIRs) provide one plausible explanation of the modulated variability that is observed in UV resonance-line P Cygni profiles (Prinja, Massa & Fullerton 1995; Fullerton et al. 1997).

As the wind structures produced by stellar rotation increase the effective wind clumping factor ($\langle N_{\rm e}\rangle^2/\langle N_{\rm e}^2\rangle$), all diagnostics of the mass-loss rate that are based on recombination (radio continuum, Hα equivalent width) will systematically overestimate the mass-loss rate. Hence a good understanding of the effect of rapid rotation on stellar wind dynamics is important not only to improve radiative-hydrodynamic models, but also to obtain more accurate mass-loss rates, which in turn has implications for the evolution models of the most massive stars (e.g. Maeder 1999).

Petrenz & Puls (1996) made the first systematic study of the influence of stellar rotation on Hα line formation. They computed line profiles in a 2D geometry and identified two important effects. The first they called the ρ^2-effect, which is essentially the increase in the recombination rate due to the wind compression (see above). The second effect was that the differential rotational velocity field near the base of the wind (where most of the Hα flux is produced) leads to a twisting of the resonance zones which alters the line profile morphology, producing a central absorption. It was found that neglect of rotation effects typically means that mass-loss rates are overestimated by 20–30 per cent, but this could increase to 70 per cent for the worst-case scenario, that of a rapid rotator viewed pole-on.

The most direct way of probing the wind geometry in the near-star regime is linear polarimetry. The copious free electrons in the wind lead to Thomson scattering, and if the wind is asymmetric, then a small but measurable continuum polarization results. Although the stellar-wind geometry cannot be uniquely recovered from the linear polarization measurements alone, a (simultaneous) comparison between models and observations of intensity line profile morphologies and linear polarization profiles should provide a strong constraint on the outflow pattern (cf. Brown et al. 1995; Harries & Howarth 1996, hereafter HH96).

In order to make full diagnostic use of the optical spectroscopic and polarimetric time-series data, it is necessary to compare the observations with the predictions of radiation-hydrodynamics models. In this paper I present a three-dimensional radiative-transfer code, TORUS, that is designed to compute synthetic spectra [in all four (I, Q, U, V) Stokes parameters] of mass-losing stars using the core–halo approximation. The code has applications in the areas of structured winds of hot stars (which are the focus of this paper), and in the modelling of spectra from the dusty envelopes of cool stars and line formation in bipolar planetary nebulae.

In the next section I describe the code in some detail, concentrating on the flow of the Monte Carlo loop and the variance reduction procedures. In Section 3 the results of several tests of the code are reported, and comparisons between the new code and proven radiative-transfer programs are illustrated. Two sample applications of the code are given in the subsequent sections, the first examining the effect of a spiral density wave on the emission-line profile, and the second the effect of a wind structure distorted by a random distribution of density enhancements. In Section 5 a new line polarization mechanism is described and compared with the spectropolarimetric observations of HH96. The results of the example applications are discussed in the final section in the context of current observational knowledge.

2 THE RADIATIVE-TRANSFER CODE

The radiative-transfer code, TORUS, was developed in Fortran 90. A modular approach was adopted, which means that different geometries and scattering processes (e.g., Mie or Rayleigh) can be incorporated into the code very simply. Monte Carlo radiative-transfer techniques were used, since these greatly simplify the computation, particularly when rotational velocity fields are being considered, which may lead to multiple resonance zones along a single line of sight. Variance reduction techniques were employed where possible, in order to increase computational efficiency.

The first stage of the code is to input the model parameters. First of these are the line emissivities and opacities of the transition as a function of wind radius [$\eta_{\rm L}(r)$ and $\chi_{\rm L}(r)$ respectively], which are computed in 1D via a statistical equilibrium code (STATEQ; Harries 1995) based on the methods of Klein & Castor (1978). The other parameters are the electron-scattering opacity $\chi_{\rm e}(r)$, the velocity law $v(r)$, the continuum flux at the line frequency f_ν, and the stellar radius R_*.

The next stage is to map the 1D line opacities and emissivities on to a 3D grid assuming spherical symmetry. Either Cartesian (x, y, z) or spherical polar (r, θ, ϕ) grids may be used, although the latter are most frequently adopted. The opacity grid is then distorted according to the selected geometrical configuration, formulated as a function of grid position $f(\boldsymbol{r})$, where $\boldsymbol{r}$ is a position vector. For example, an oblate envelope could be constructed using

$$f(\boldsymbol{r}) = (1 - \mu^2), \tag{1}$$

where $\mu = \cos\theta$. For recombination lines (e.g., Hα) it is assumed that the opacity and emissivity scale as density squared, while the electron-scattering opacity scales linearly with density. So we have

$$\eta_{\rm L}(\boldsymbol{r}) = \eta_{\rm L}(r) f^2(\boldsymbol{r}),$$
$$\chi_{\rm L}(\boldsymbol{r}) = \chi_{\rm L}(\boldsymbol{r}) f^2(\boldsymbol{r}),$$
$$\chi_{\rm e}(\boldsymbol{r}) = \chi_{\rm e}(\boldsymbol{r}) f(\boldsymbol{r}). \quad (2)$$

At this point the velocity field, which is assumed to be purely monotonic and radial initially, may be modified (e.g., by the inclusion of azimuthal terms due to rotation).

When the opacity and velocity grids are complete, it is necessary to construct probability density functions so that the locations of the line emission can be correctly computed. For the spherical polar grid case the probability density function $u(r)$ for that a line photon produced at radius less than r is

$$u(r) = \frac{\int_{r_{\rm min}}^{r}\int_0^{\pi}\int_0^{2\pi}\eta_{\rm L}(r,\theta,\phi) r^2 \sin\theta\,{\rm d}\phi\,{\rm d}\theta\,{\rm d}r}{\int_V \eta_{\rm L}(r,\theta,\phi)\,{\rm d}V}, \quad (3)$$

where $r_{\rm min}$ is the minimum wind radius, and V represents the entire wind volume. It is then necessary to compute, for each radial grid step r, a probability density function for the polar angle θ:

$$u(r,\theta) = \frac{\int_0^{\theta}\int_0^{2\pi}\eta_{\rm L}(r,\theta,\phi)\sin\theta\,{\rm d}\phi\,{\rm d}\theta}{\int_0^{\pi}\int_0^{2\pi}\eta_{\rm L}(r,\theta,\phi)\sin\theta\,{\rm d}\phi\,{\rm d}\theta}. \quad (4)$$

Finally, for each polar angle grid step, at each radial grid step, a probability density function for the azimuthal angle ϕ must be computed:

$$u(r,\theta,\phi) = \frac{\int_0^{\phi}\eta_{\rm L}(r,\theta,\phi)\,{\rm d}\phi}{\int_0^{2\pi}\eta_{\rm L}(r,\theta,\phi)\,{\rm d}\phi}. \quad (5)$$

From the above these distributions, and three random numbers chosen from a uniform distribution between 0 and 1, the location (r,θ,ϕ) of a line photon emission can be determined.

The resulting code follows a simple loop over the number of photons, with the following steps.

(i) Is this photon from the line or continuum? The probability that a photon is a line photon, $p_{\rm l}$, is computed from

$$p_{\rm l} = \frac{\int_V \eta_{\rm L}(\boldsymbol{r})\,{\rm d}V}{\int_V \eta_{\rm L}(\boldsymbol{r})\,{\rm d}V + 4\pi R_*^2 \int_{\nu_1}^{\nu_2} f_\nu\,{\rm d}\nu}, \quad (6)$$

where R_* is the radius of the stellar photosphere, ν_1 and ν_2 are the lower boundaries of the section of spectrum being modelled, and f_ν is the continuum flux.

Each continuum photon packet was chosen to represent $N_{\rm bin}$ frequency bins spaced between ν_1 and ν_2. Associated with each bin is a weight, which describes the attenuation of the packet at that frequency by line absorption. Hence, in following a single photon trajectory, $N_{\rm bin}$ photons are treated simultaneously, leading to a great improvement in the variance of the continuum at the expense of highly correlated errors between continuum bins (cf. Hillier 1991).

In order to increase the statistical efficiency of the code, a fraction, $x_{\rm l}$, of the total number of photons in the run were selected to be line photons. Each line photon was then reweighted by

$$w_{\rm l} = p_{\rm l}/x_{\rm l}, \quad (7)$$

and each continuum photon by

$$w_{\rm c} = \frac{1-p_{\rm l}}{N_{\rm bin}(1-x_{\rm l})}. \quad (8)$$

(ii) The position of this photon is computed. If it is a line photon, then this is done using equations (3), (4) and (5), otherwise the Cartesian position vector $\boldsymbol{r}$ on the stellar photosphere is computed from

$$w = 2t_1 - 1,$$
$$u = \cos(2\pi t_2)\sqrt{(1-w^2)},$$
$$v = \sin(2\pi t_2)\sqrt{(1-w^2)},$$
$$\boldsymbol{r} = (uR_*, vR_*, wR_*), \quad (9)$$

where t_1 and t_2 are uniform random deviates.

(iii) A numerical integration through the grid to the observer (in direction $\hat{\boldsymbol{u}}$) is performed to compute the optical depths. This is the most computationally expensive part of the algorithm, requiring grid searches and interpolations in three dimensions. The projected speed of the wind material v_p with respect to the rest frame of the emitting atom $\boldsymbol{v}_{\rm r}$ and the bulk velocity of the wind $\boldsymbol{v}_{\rm w}$ are calculated at each of the integration steps from

$$v_p = (\boldsymbol{v}_{\rm w} - \boldsymbol{v}_{\boldsymbol{r}}) \cdot \hat{\boldsymbol{u}}, \quad (10)$$

where $\boldsymbol{v}_{\rm w}$ is the local wind velocity. The resonance zone then occurs when

$$\frac{\nu_0 - \nu_{\rm r}}{\nu_0} = \frac{v_p}{\rm c}, \quad (11)$$

where ν_0 is the rest frequency of the line transition, and $\nu_{\rm r}$ is the frequency of the photon in the rest frame of the emitting atom. The Sobolev optical depth is given by

$$\tau_{\rm sob} = \frac{\chi_{\rm l}}{\nu\left|{\rm d}(\hat{\boldsymbol{u}}\cdot\boldsymbol{v})/{\rm d}\hat{\boldsymbol{u}}\right|}, \quad (12)$$

where $\boldsymbol{v}$ is the velocity at the resonance zone. The denominator contains the line-of-sight velocity gradient, which is computed numerically in TORUS in order that the code remains as general as possible. The chance of a line photon emerging after emission is given by the angle-dependent Sobolev escape probability,

$$p_{\rm esc} = \frac{1-\exp(-\tau_{\rm sob})}{\tau_{\rm sob}}. \quad (13)$$

The probability that a line photon reaches the observer is then

$$\frac{1}{4\pi} p_{\rm esc}\exp(-\tau_{\rm sob})\exp(-\tau_{\rm es}), \quad (14)$$

while for a continuum photon it is

$$\frac{1}{\pi}\exp(-\tau_{\rm sob})\exp(-\tau_{\rm es})\hat{\boldsymbol{u}}\cdot\hat{\boldsymbol{r}}, \quad (15)$$

where $\hat{\boldsymbol{r}} = \boldsymbol{r}/|\boldsymbol{r}|$.

The photon flux is then added to the output arrays, appropriately weighted by the probabilities and taking into account the Doppler shift from the scattering electron's rest frame to that of the observer [see (vii)].

(iv) For line photons the emission process is isotropic, and a random photon direction ($\boldsymbol{u}'$) is the chosen. In the case of a continuum photon, this direction must be outwards from the photosphere (i.e., $\hat{\boldsymbol{u}}'\cdot\hat{\boldsymbol{r}} > 0$), and the photon must be reweighted by $2\hat{\boldsymbol{u}}'\cdot\hat{\boldsymbol{r}}$.

(v) The numerical integration is performed along the random photon path to the grid boundary. The photon is forced to scatter before the grid boundary. If the scattering optical depth to the boundary is τ_∞, then the optical depth to scattering, τ_{es}, is then

$$\tau_{es} = -\ln\{1 - t[1 - \exp(-\tau_\infty)]\}, \quad (16)$$

where t is a uniform random deviate between in the range [0,1]. The photon must then be reweighted by $1 - \exp(-\tau_\infty)$, and also by $\exp(-\tau_{sob})$. The position of the first scattering event is then found.

(vi) The probability that the photon is scattered towards the observer is found from the phase matrix. The integral through the wind to the observer is performed in order to obtain τ_{sob} and τ_{es}. The photon is added to the output arrays, weighted by the factor

$$\frac{1}{4\pi}\exp(-\tau_{sob})\exp(-\tau_{es}) \quad (17)$$

and taking into account the appropriate Doppler shift between the scattering electron and the observer's rest frame [see (vii)].

(vii) The new photon direction is computed according to the scattering phase matrix, and the Stokes intensities are calculated according to the scheme adopted by Hillier (1991, appendix C), which is in turn based on that by Chandrasekhar (1960). If $\boldsymbol{v}_{\mathbf{new}}$ and $\boldsymbol{v}_{\mathbf{old}}$ are the new and old velocities velocities respectively, then the new photon frequency (ν_r) in the rest frame of the electron is computed from

$$\nu_r = \nu_{old}\frac{\sqrt{1 - v^2/c^2}}{1 + v'/c}, \quad (18)$$

where

$$v = |\boldsymbol{v}_{\mathbf{new}} - \boldsymbol{v}_{\mathbf{old}}| \quad (19)$$

and

$$v' = (\boldsymbol{v}_{\mathbf{new}} - \boldsymbol{v}_{\mathbf{old}}) \cdot \hat{\boldsymbol{n}},$$

where $\hat{\boldsymbol{n}}$ is the incoming photon direction.

A fixed number of scatterings [stages (v) to (vii)] can be forced before the photon is allowed to escape. In the regime of the O-supergiant winds, with electron-scattering optical depths of $\sim$0.1, two scatterings are forced, principally to achieve a variance reduction in the continuum polarization quickly.

(viii) The code loops back to the compute the next photon path.

Using the variance reduction techniques described, the required signal-to-noise ratio (an accuracy of 0.1 per cent in polarization magnitude per bin) for a model (200 velocity bins) is achieved with 10^6 photon packets. Computation times for such calculations are of transitory value, given the rapid development of computing power, but contemporary readers should note that 10^6 photons take approximately one hour to run on a 400-MHz DEC alpha workstation.

3 CODE TESTING

As a base model for both the code testing and the example applications, the parameters of the O4 I(n)f (Walborn 1972) star ζ Puppis were adopted, primarily because it is rapidly rotating ($v_{rot} = 219\,km\,s^{-1}$; Howarth et al. 1997), is intrinsically polarized (HH96), and has been extensively studied using high-resolution time-series spectroscopy in the optical (e.g. Reid & Howarth 1996; Eversberg, Lépine & Moffat 1998, hereafter ELM98). Three different periods have been found in the line-profile variations of ζ Puppis. The longest period, found both in Hα (Moffat & Michaud 1981) and UV P Cygni profiles (Howarth et al. 1995) as well as X-rays (Berghöfer et al. 1996), is 5.1 d, which is the likely rotation period. The second period, 15–19 hr, is less strictly periodic, and is rather the recurrence time-scale for discrete absorption components. The shortest period, 8.54 hr, was found in the photospheric absorption lines and may be attributable to non-radial pulsations with $l = -m = 2$ (Reid & Howarth 1996). The physical parameters used for ζ Puppis are listed in Table 1.

The initial tests were performed in order to compare the TORUS line profiles with those computed using established radiative-transfer codes. The first of these, LINPRO (Harries 1995), computes line profiles according to the 1D prescription of Castor (1970). Since electron-scattering opacity is neglected in this treatment, and the electron-scattering optical depth of the test model is significant ($\tau_{es} \sim 0.15$), the electron-scattering opacities were artificially set to zero for this test. No core absorption profile was included for this comparison, once again due to limitations of the LINPRO code. The comparison tests TORUS in its simplest configuration – that of a spherical outflow with purely radial velocity fields without electron scattering. The two line profiles (see Fig. 1a) show satisfactory agreement.

In the second set of tests I employed the ELEC code (Hillier 1991) modified by Harries (1995) to incorporate core–halo geometries. This is based on the Monte Carlo approach and uses a 1.5D geometry, in which axisymmetric density distortions may be incorporated without changes to the spherical velocity law. We adopted a simple latitudinal density structure

$$f(\mu) = k(1 - x\mu^2), \quad (21)$$

where x is a density contrast factor, and k is a normalization factor, chosen so to conserve the mass-loss rate compared to the undistorted model. The line emissivities and opacities (which result from recombination processes) were scaled according to equation (2). The velocity law was not altered (this was necessary, since ELEC requires monotonic velocity laws along all sightlines). A comparison between the line profiles produced by the two codes once again shows good agreement, with very minor differences at low velocities due to the different interpolation schemes adopted (Fig. 1b).

Further tests were performed in order to gauge the accuracy of the computed polarization. The first test is to ensure that a spherical geometry produces no net polarization (to within the statistical errors inherent in the Monte Carlo technique). Several runs of $\sim 10^6$ photons were calculated adopting a spherical geometry, in order to confirm that the continuum polarization was indeed zero.

Table 1. Physical parameters adopted for ζ Puppis. The references are (1) Bohannan et al. (1986), (2) Abbott & Lucy (1985), (3) Puls et al. (1996), (4) Howarth et al. (1997), (5) Pauldrach et al. (1994) and (6) this study.

Parameter (unit)	Value	Reference
Effective temperature, T_{eff} (K)	42 000	1
Radius, R ($R_\odot$)	19	5
Rotational velocity, $km\,s^{-1}$	219	4
Gravity, $\log g$ (cgs dex)	3.5	1
Mass-loss rate, $\dot{M}$ ($M_\odot\,yr^{-1}$)	5×10^{-6}	2
Wind base velocity, v_0 ($km\,s^{-1}$)	100	6
Terminal velocity, v_∞ ($km\,s^{-1}$)	2250	3
Inclination, i (°)	90	6
Acceleration law, β	1.15	3

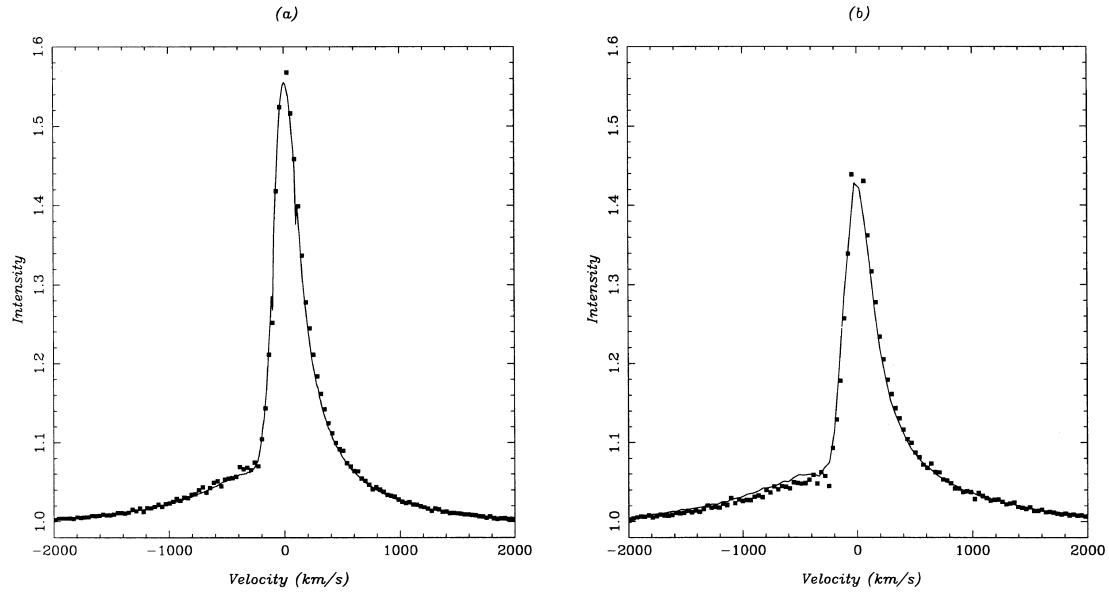

Figure 1. Tests of the TORUS code. (a) shows a comparison between Hα profiles computed using an analytical approach (solid line) and TORUS (filled squares) with the electron-scattering opacity set to zero (see text). (b) shows a similar comparison, this time between TORUS (filled squares) and ELEC (solid line).

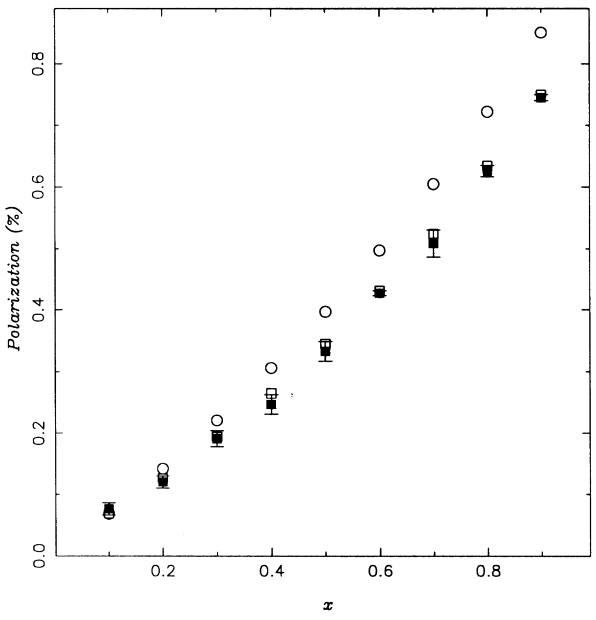

Figure 2. A comparison between continuum polarizations computed using TORUS (filled squares), ELEC (open squares), and the Fox analytical model (open circles). The models were computed using a latitudinal density structure $f(\mu) = k(1 - x\mu^2)$ (see text), and x is plotted along the abscissa, while the ordinate shows the corresponding continuum polarization.

Additional models were computed adopting the density structure of equation (21), and the continuum polarization was compared with that predicted using the single-scattering analytical model of Fox (1991) and ELEC. The Fox model is an extension of the work by Brown & McLean (1977), taking into account the finite size of the stellar source and occulation by the core. I computed a grid of nine models (corresponding to $x = 0.1, 0.2, 0.3, \ldots, 0.9$) using TORUS, ELEC, and the Fox model. The polarizations computed using the two Monte Carlo codes are in excellent agreement (see Fig. 2), but even at the relatively low scattering depths of our test model ($\tau \sim 0.15$) multiple scattering affects the polarization (see, e.g., Harries 1995), and the analytical model systematically overestimates the continuum polarization. Tests were conducted with the mass-loss rate reduced by an order of magnitude, bringing the models well into the regime of applicability of the single-scattering analysis. For these models the agreement between the Fox model and TORUS was very good.

The results of the above tests indicated that the code behaves as expected, and that its results can be treated with confidence.

4 APPLICATIONS OF TORUS

In order to illustrate the possible applications of the code, I have computed synthetic polarized line profiles for ζ Puppis using two distinct models for the wind geometry. The physical parameters adopted were the same as for the tests (see Table 1), but instead of assuming a flat continuum through Hα, a core absorption profile was adopted, taken from the model grid described by Smith & Howarth (1994).

In the first case I consider a spherical wind structure modified by a spiral streamline of enhanced density, while in the second instance I examine the effect of random blobs propagating through the wind.

4.1 Corotating spiral structures model

As noted in the introduction, the absorption troughs in the UV P Cygni profiles of some hot stars have been found to vary periodically with the stellar rotation period. This implies that some large-scale wind structures are seeded by the photosphere. Hydrodynamical models have demonstrated that a localized increase in mass-loss rate, resulting say from a photospheric hotspot, leads to a spiral density enhancement (Cranmer & Owocki 1996), and such models have been used to explain the line-profile variability of the rapidly rotating B0.5Ib star HD 64760 (Prinja et al. 1995; Fullerton et al. 1997).

The equation of the spiral streamline in the equatorial plane

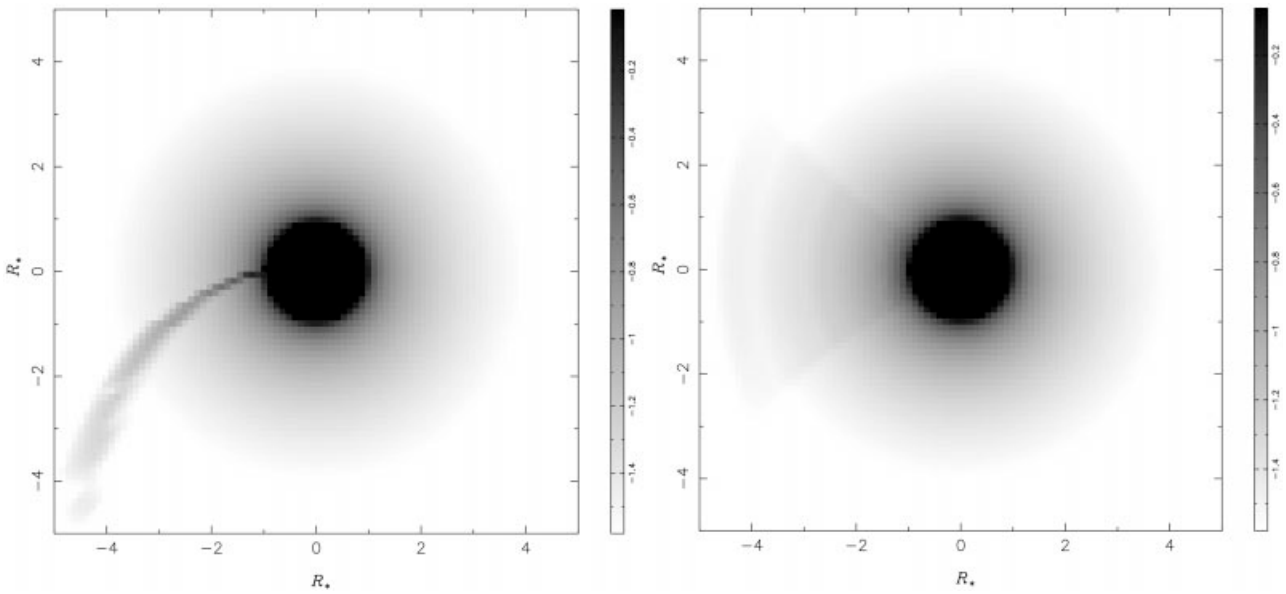

Figure 3. The electron-scattering optical depth distribution of the spirally distorted wind. The left-hand panel shows the distribution of optical depths as viewed along the rotational axis of the star (rotating in the clockwise sense in this image). The logarithmic intensity scale is given on the immediate right-hand side of the image. The right-hand grey-scale shows the system viewed edge-on ($i = 90°$), which is the configuration used to compute the model line profiles.

(Cranmer & Owocki 1996; Fullerton et al. 1997) is

$$\phi(r) = \phi_0 - \frac{v_{\rm rot}}{v_\infty} I(r, w_0, \beta), \tag{22}$$

where $\phi_0 = \phi(r = 1)$, I is given by

$$I(r, w_0, \beta) = \int_{R_*}^{r} \frac{1 - (R_*/r)^2}{w_0 + (1 - w_0)(1 - R_*/r)^\beta} {\rm d}r, \tag{23}$$

and $w_0 = v_0/v_\infty$. The latitudinal extent of the spiral structures was not computed by Cranmer & Owocki, since this requires extension of the hydrodynamical calculations into three dimensions. I make the pragmatic assumption that the spiral structure lies on the range $60° \leq \theta \leq 120°$. The thickness of the spiral, perpendicular to the spiral path, is assumed to be $0.1r$, while its density contrast (relative to the local wind material) is taken to be a factor of 5 (based on the density contrast seen in the hydrodynamical models of Cranmer & Owocki). The velocity field of the grid was adjusted to include the azimuthal terms produced by the conservation of angular momentum from the wind base. The azimuthal velocity as a function of radius and polar angle is given by

$$v_\phi(r, \theta) = v_{\rm rot} \frac{R_*}{r} \sin\theta. \tag{24}$$

The models were computed on a spherical polar coordinate mesh comprising 60 logarithmically spaced radial steps, 200 polar angle steps (evenly spaced in $\cos\theta$), and 200 evenly spaced azimuthal steps. A total of 50 spectra were computed, corresponding to one complete rotation of the spiral structure.

The 50 model spectra were first added together to produce a mean profile, which was then divided into each of the model profiles to yield quotient spectra. The dynamic nature of the data set is most easily visualized as a grey-scale of these quotient spectra (see Fig. 4). The maximum variations of the individual profiles from the mean is $\sim \pm 5$ per cent. Examining the quotient spectra close to phase 0 (which corresponds to the image in the right-hand panel of Fig. 3), it can be seen that there is enhanced emission slightly redwards of the line centre. At this phase the spiral base is at nearly 90° to the observer (hence the projected velocities are close to zero), and is curving towards the observer, leading to a small amount of blueshifted emission in the observer's frame. As the star rotates, the spiral begins to turn away from the observer, and we observe a redwards acceleration of the line emission as the emission from the spiral is formed in the part of the wind receding the observer. When $\phi \approx 0.35$, the spiral is pointing almost directly away from the observer, and we see the greatest distribution of projected velocities. The emission from the spiral is also slightly reduced at these phases, since the spiral is passing behind the stellar core. Beyond $\phi = 0.35$, the spiral emission is observed to accelerate to lower velocities until at $\phi \approx 0.5$ the enhanced emission is blueshifted. Also at this phase the dense wind base is just being observed on the approaching limb of the star (at a velocity of $-v_{\rm rot}$). As the star rotates, this low-velocity feature passes across the stellar disc and disappears behind the receding limb.

The variability as a function of phase is clearly observed in the line equivalent width (Fig. 5) with maximum emission at phases 0 and 0.5, and minima at phases 0.25 and 0.75 (the $\phi \sim 0.25$ minimum is deeper, since this is the phase at which the base of the spiral is eclipsed by the core).

The velocity of the peak enhancements in the quotient spectra were measured by using the DIPSO spectral analysis program (Howarth et al. 1998). There are two extended periods per rotation where the acceleration is nearly constant, and there is a linear trend of velocity with rotational phase. A linear least-squares fit to the velocity as a function of time (assuming that one rotation corresponds to 5.1 d) for these two datatrains yields an acceleration/deceleration of $0.01\,{\rm km\,s^{-2}}$.

The line profile variation (lpv) pattern produced the the one-arm spiral distortion cannot explain the observed variations of ζ Puppis alone, but it should be remembered that Reid & Howarth (1996)

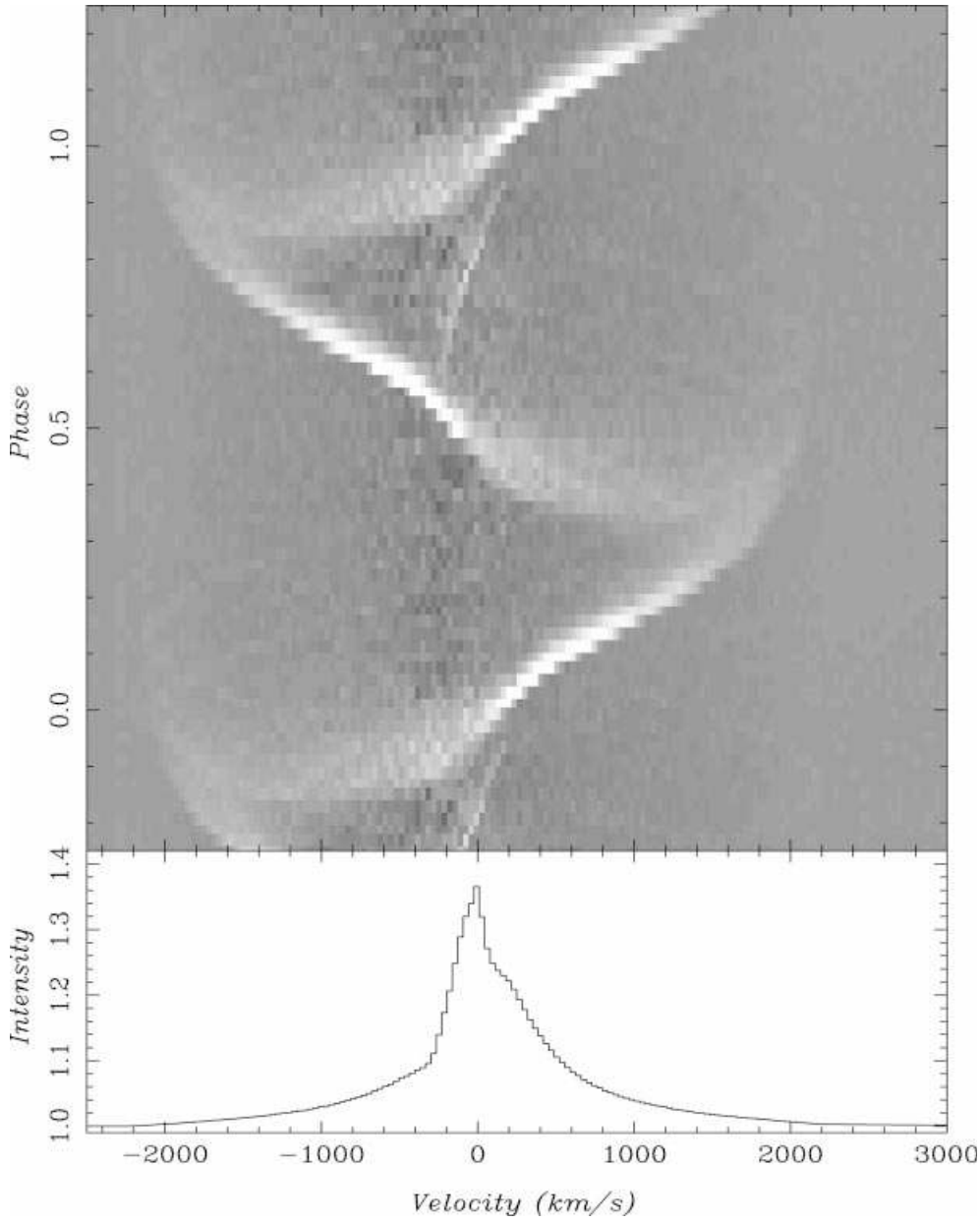

Figure 4. The results of the spiral model. The top panel shows the evolution of the line profile with stellar rotation. The *x*-axis is the velocity, the *y*-axis is the rotational phase, and the intensity of the quotient spectrum is given by the grey-scale intensity, scaled between 0.95 (black) and 1.05 (white). The bottom panel displays the corresponding mean Hα spectrum.

observed both accelerating and decelerating features in the Hα absorption component, and such lpvs *cannot* be explained purely in terms of radially propagating blobs, which will generally be observed as emission enhancements accelerating away from the line centre (but see Section 4.2). Furthermore, although the accelerations measured from the model spectra are quite low, they could be mistaken for blobs that were propagating approximately tangentially to the observer's line of sight.

The continuum polarization of the models is presented in Fig. 5. The maximum polarization occurs just after phases $\phi = 0$ and 0.5, which correspond to a configuration in which the spiral arm is tangential to the observer's line of sight (see Fig. 3). The polarization magnitude is maximum here as the core-spiral arm–observer angle is close to 90°, giving the largest polarization according to the Rayleigh scattering phase matrix. Conversely, minimum polarization occurs close to phases $\phi = 0.25$ and 0.75, at which the spiral arm is pointing towards (or away from) the observer. The configuration here is such that the (very small) polarization results from scattering above and below the core, leading to a polarization position angle that is perpendicular to that observed at $\phi = 0$ [hence $\bar{q} = (Q/I)$ is negative]. (The most negative $\bar{q}$ values are observed at $\phi \approx 0.25$ when only the upper and lower portions of the spiral arms are visible to the observer.)

Time-series analysis of the UV resonance line profiles of HD 64760 revealed a convex downward pattern of the Fourier phase across the line profile at the peak frequency, the so-called 'phase bowing' (Fullerton et al. 1997). The bowed shape indicates that the wind variability is evolving to both smaller and larger

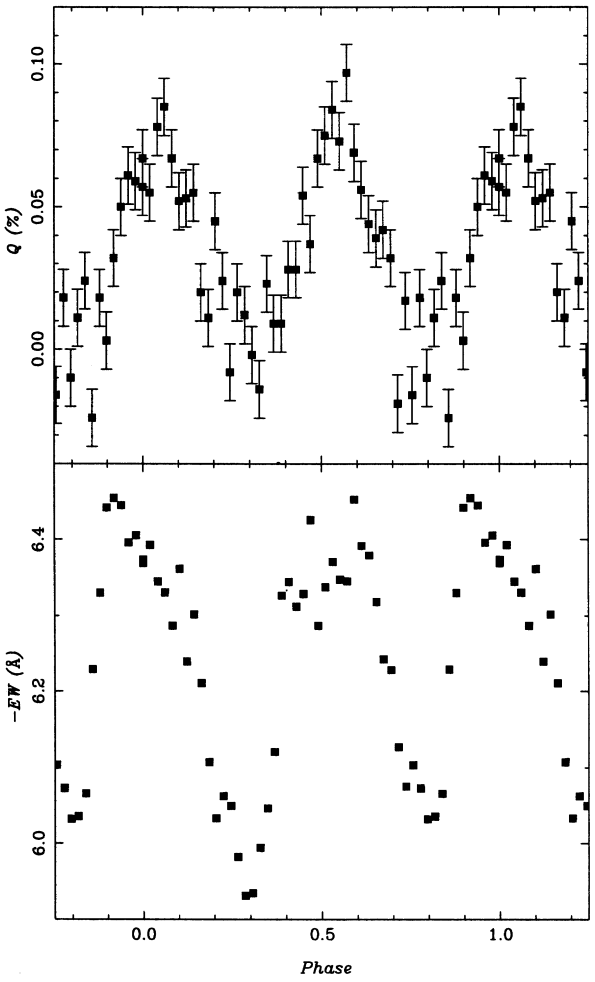

Figure 5. The polarization and line equivalent widths produced by the spirally distorted wind. The abscissa shows the rotational phase, while the top panel displays the normalized Stokes Q parameter. Reflective symmetry about the model's equatorial plane means that $U = 0$ at all phases. The bottom panel shows the equivalent width of the line, with the zero-point truncated in order to emphasize the variability (an amplitude of about 10 per cent).

projected velocities, and is most simply interpreted as arising from absorption by corotating spiral streams projected against the stellar disc (Owocki, Cranmer & Fullerton 1995). A Fourier analysis was performed on the synthetic time-series, after concatenating five cycles in order to simulate an extensive dataset. In Fig. 6 the Fourier phase of the frequency maximum (1 rotation^{-1}) is plotted against projected velocity. Phase bowing is clearly observed, with the red and blue sides of the profile 180° out of phase, as expected in this simple one-arm spiral case. Increasing the number of spiral arms naturally leads to a more complex dynamic spectrum, with a crosshatch effect as the emission from the individual spiral arms coincides in velocity space, although phase bowing is still observed at the peak frequency.

4.2 Clumpy model

High signal-to-noise time-series spectroscopy of the He II λ4686 emission line of ζ Puppis by ELM98 showed low-level (~2 per cent of the continuum) lpvs produced by discrete emission-line 'bumps' that were observed to migrate away from the line-centre, towards both the red and blue wings. The lpvs were reminiscent of those observed in Wolf–Rayet stars, which are thought to result from the propagation of density enhancements (or 'blobs') through the wind (Robert 1992). It was noted by ELM98 that since no lpvs were seen to accelerate *towards* the line centre, it was unlikely that they resulted from large-scale corotating structures, which would show an 'S-wave' pattern with time (cf. Fig. 4).

Only a few discrete bumps were seen in the ELM98 time-series, perhaps corresponding to the largest and/or densest clumps in the wind (but see later). There are currently few constraints on either the size or density contrast of the blobs, although work on the theoretical framework for deducing such parameters from combined spectrocopic and photopolarimetric observations has begun (Brown et al. 1995; Richardson, Brown & Simmons 1996). I adopted a factor of 50 density contrast, which is comparable to that estimate for the clumps in the cool winds of AGB stars (~30; Richards, Cohen & Yates 1997). The size scale of each blob was

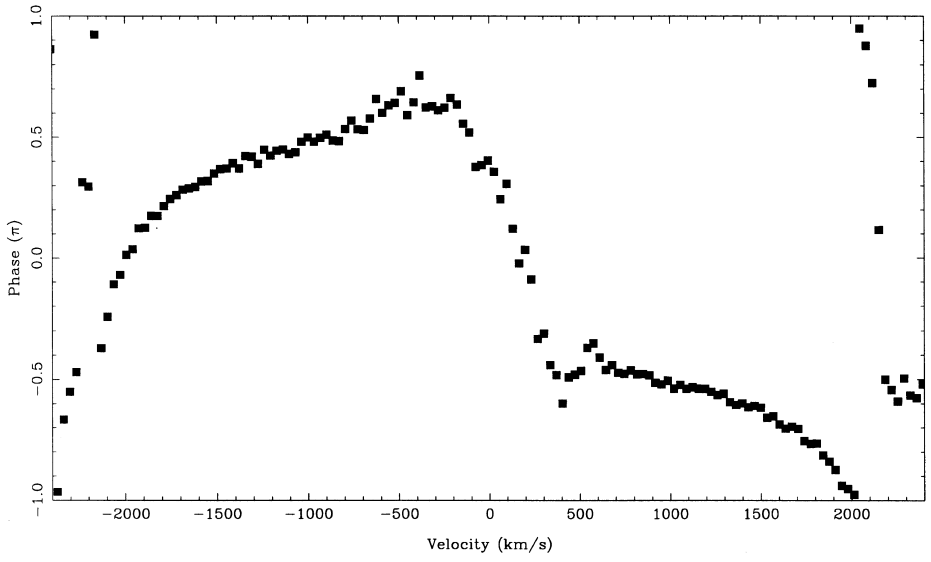

Figure 6. Fourier phase (in terms of π) of the rotational modulation for the corotating spiral structure model plotted as a function of projected velocity.

chosen to have a random value between 0.01 and 0.1 stellar radius, and the spherically symmetric blobs were assumed to have a 3D Gaussian density distribution, with a FWHM of the scalelength. This corresponds to a hierarchy of blob sizes with $N(r_{\rm blob}) \propto r_{\rm blob}^{-3}$. It was assumed that the blobs follow the velocity field of the ambient wind, which includes an azimuthal component given by equation (24).

I made the assumption that on average one blob is produced every 2 hours, and that the blobs are produced at the wind base. (Brown 1994 has shown that the redistribution or condensation of electrons into blobs above the photosphere will result in no net polarization.) The model was started with no blobs, and at each time interval Poisson statistics were used to determine the number of new blobs, which were initially placed randomly at the stellar surface. A numerical integration of the blob velocity vectors was performed at each time-step in order to determine the new blob positions. Blobs that reached 10 stellar radii (which had negligible total emissivity or opacity) were removed from the computation, and it was found that after a time period long compared to the wind-flow time-scale there were typically 10 blobs located between the stellar photosphere and 10 stellar radii (a 'snapshot' blob configuration is shown in Fig. 7). After the code had simulated the blob dynamics over several wind-flow times, spectra were computed at each time interval. A total of 50 spectra were computed, spanning a time interval of 24 hours.

A mean spectrum was computed from the 50 models, and this was divided into each individual profile to yield the dynamic spectrum plotted in Fig. 8. Four clear emission features are seen accelerating away from the line centre, and no variability is observed beyond $\pm 1000\,{\rm km\,s^{-1}}$, in agreement with the ELM98 observations.

One of the most obvious properties of the simulation is that at least two out of the four observed emission features result from the superposition in velocity space of the flux from multiple wind blobs (see the continuous lines plotted over the grey-scale in Fig. 8). Only the third strong feature (which appears at 5×10^4 s) unambigously arises from a discrete wind blob. It is probable that the second feature (the redwards accelerating feature at 4×10^4 s) is also produced by a single blob, since the feature appears abruptly at $v \sim 300\,{\rm km\,s^{-1}}$ as it emerges from behind the stellar core.

Interestingly, the acceleration curve of an apparently single emission-line bump measured by ELM98 showed a discontinuity, which the authors attributed to the velocity superposition described above. The bias induced by assigning a one-to-one correspondence between emission bumps in spectra and individual wind clumps has been discussed by Lépine, Moffat & Henriksen (1996) and Lépine & Moffat (1999).

Gaussian profiles were fitted to the emission bumps in each of the model profile spectra, to provide velocities and velocity FWHM. The velocities of each feature were well fitted by a linear acceleration, simply because the Hα formation region ($<2R_*$) covers only a small fraction of the accelerating zone, and in this region the β-law is well approximated by a single-valued acceleration. This, combined with the degeneracy caused by projection effects and the fact that the strongest features result from the blending of several independent wind blobs, means that a reliable estimate of the velocity law from Hα measurements alone is fraught with difficulty (cf. fig. 6 of ELM98).

A final point is that since the wind is rotationally distorted, and it is assumed that the blobs propagate with the ambient material, it is possible for a blob to accelerate across the line centre. The initial blob velocity is dictated by the rotational velocity field at the wind base, which rapidly becomes radial as the line-driving takes over. The paths of several 'centre crossing' blobs are drawn in Fig. 8, although since these are close to the line centre they are, of course, difficult to observe.

The polarization produced by the blobs is small (Fig. 9) with an amplitude of about 0.1 per cent. The production and migration of the blobs through the wind leads to a surprisingly smooth trend in normalized Q and U. There is no correlation between equivalent width and polarization for this model.

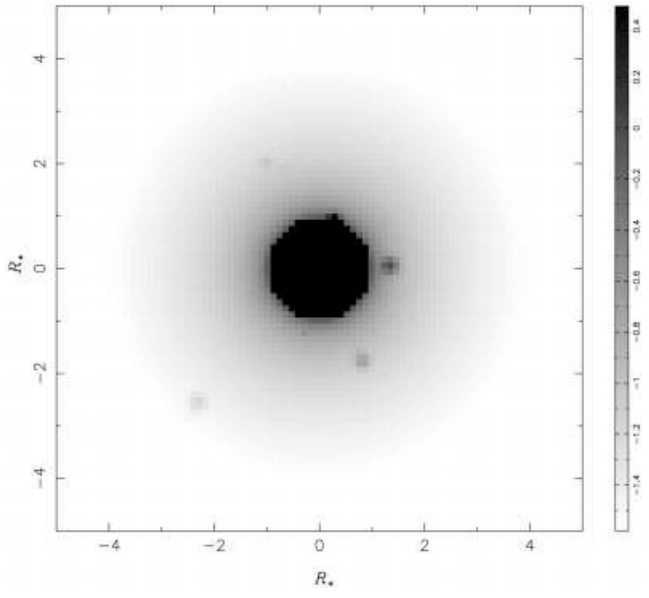

Figure 7. A grey-scale image showing logarithmically scaled electron-scattering optical depth for a typical clumpy model. The axes are distance in units of stellar radii. Several blobs can be clearly seen.

5 THE EFFECT OF ROTATIONAL VELOCITY FIELDS ON THE POLARIZED LINE PROFILE

In the simple case of a spherically symmetric wind with a purely radial flow the observer views the scattering geometry as circularly symmetric at all velocities and inclinations, and zero polarization is observed at every wavelength in both the continuum and the spectral line. However, what would be the effect of a rotational velocity field? Clearly, the symmetry will be broken (barring the pole-on views), and although the continuum polarization will remain at zero, some polarization structure might be expected in the line.

A high signal-to-noise model was computed using the ζ Puppis parameters, retaining spherical symmetry but adopting the rotational velocity field detailed in equation (24), which is based on the conservation of angular momentum. (Of course, such a combination of spherical density structure and rotational velocity field is not self-consistent, in that it violates the mass conservation equation, but it is satisfactory for illustrative purposes.)

The model geometry has reflective symmetry in the plane containing the equator, and the Stokes U parameter cancels. The Stokes Q parameter does indeed show some structure through the line (Fig. 10), comprising a narrow peak (reaching a maximum polarization of $\sim$0.1 per cent, apparently symmetric about $v =$

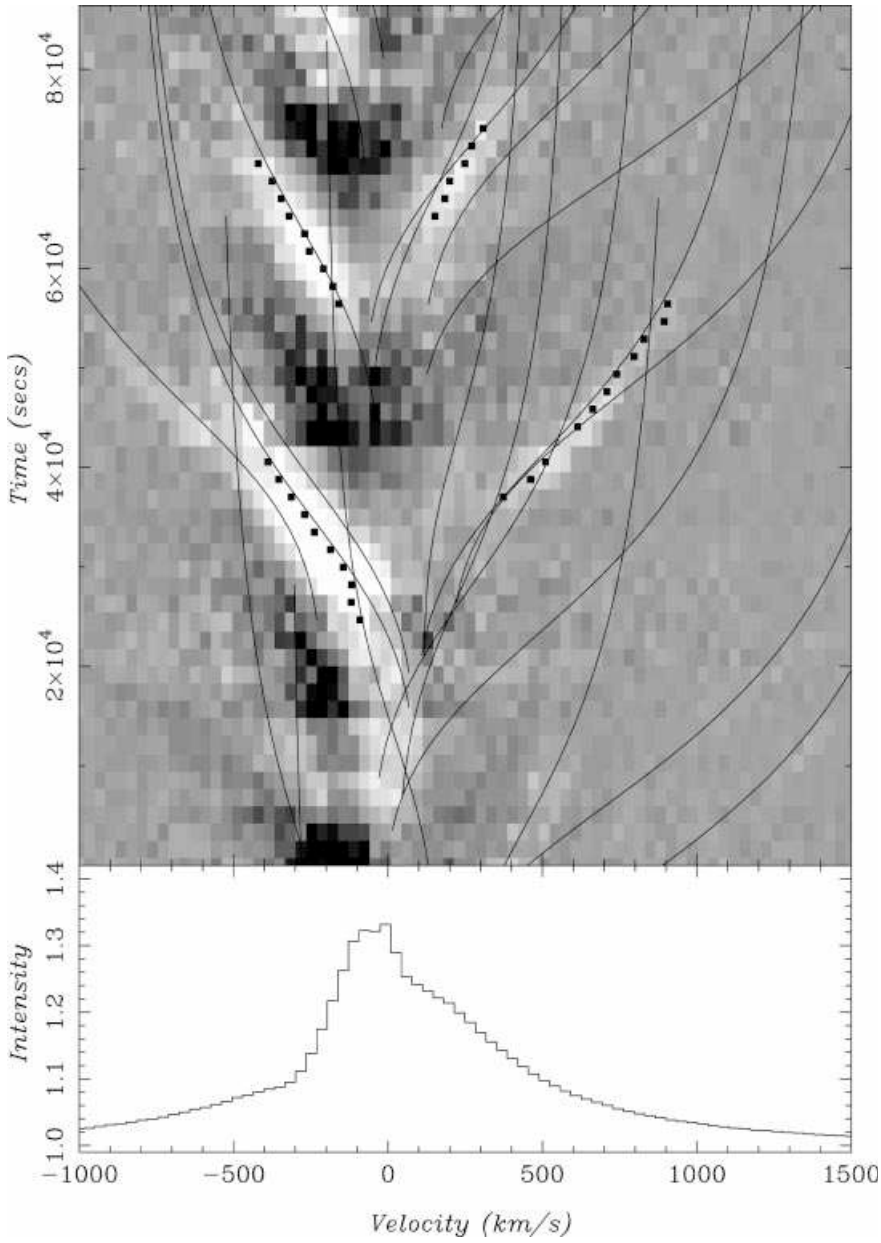

Figure 8. Synethic line profiles for the clumpy wind model. The grey-scale in the upper panel shows velocity (*x*-axis) against time (*y*-axis), while the spectral intensity relative to the mean spectrum is depicted as grey-scale levels, scaled between 0.94 (black) and 1.04 (white). The measured velocities of the accelerating components are plotted as solid squares, while the paths of *all* the blobs propagating through the wind are shown as solid lines. The lower panel shows the mean spectrum.

$0\,\mathrm{km\,s^{-1}}$) flanked by two 'dips', reaching a polarization of -0.05 per cent (which corresponds to a polarization direction parallel to the equator) at about $v \sim 200\,\mathrm{km\,s^{-1}}$ (which is approximately the equatorial rotation speed). Further models, computed at different rotational velocities, displayed a very similar polarization morphology, although it was found that the maximum polarization of the peak increased with increasing equatorial rotational velocity, and the polarization 'dips' always occurred at approximately v_{rot}. As expected, the polarization structure disappears when the wind is viewed along the angular momentum axis.

The origin of the effect is subtle. Scattering electrons at different latitudes will 'see' a different incident spectrum: those at the pole will see an unbroadened profile, while the effect of rotational broadening will be greatest at the equator. The primary differences between the profiles arises from variations in the velocity distribution of line absorption of continuum photons (cf. the resonance zone effect; Petrenz & Puls), although models run with line absorptions set to zero also show polarization structure at a much reduced level due to the latitudinal dependence of the line escape probability.

The sensitivity of the effect to other model parameters was investigated. Since the origin of the effect lies close to the wind base, it is natural to suppose that it may depend on the wind base velocity, v_0, which in the reference model ($100\,\mathrm{km\,s^{-1}}$) is significant compared with the rotational velocity. A second

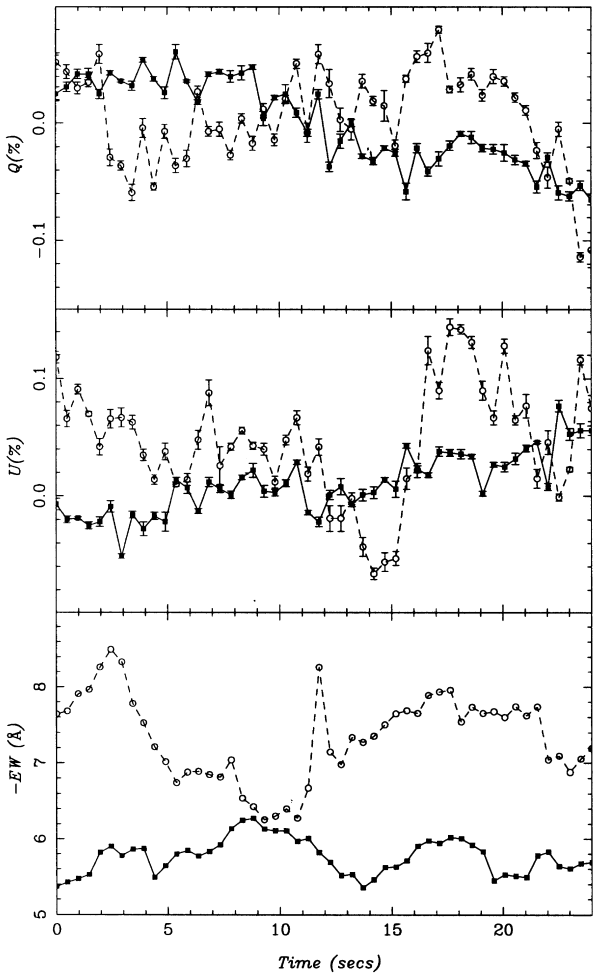

Figure 9. The continuum polarization and line equivalent width produced by the clumped-wind model. Normalized Stokes Q (top panel), Stokes U (middle panel), and equivalent width (bottom panel) are plotted against rotational phase (solid line). Results for a second series of models (see Section 6), with a blob production rate of 15 min, are also shown (dashed line).

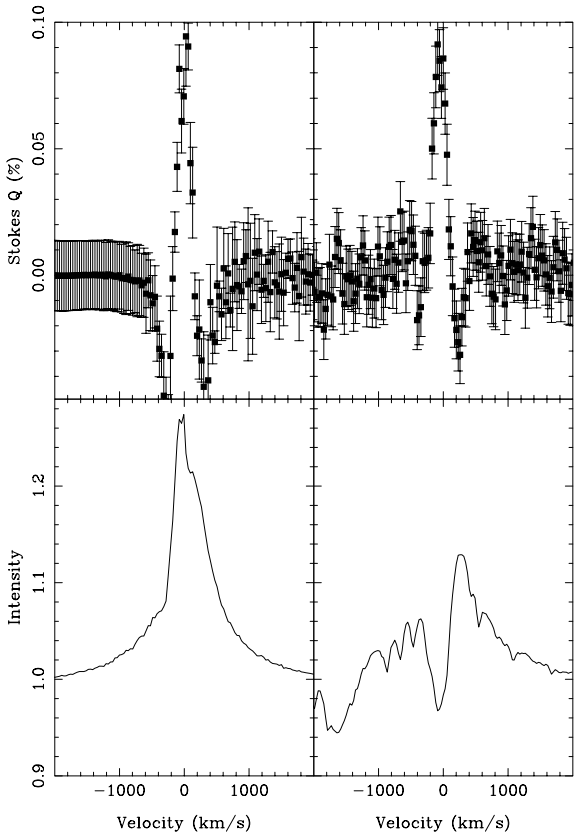

Figure 10. The lower panels display line intensity profile relative to the continuum (in velocity space), while the normalized Stokes Q parameter is plotted as a percentage in the upper panels. The left-hand figure shows the model detailed in the text, while the right-hand figure is the mean polarization spectrum of ζ Puppis (HH96) after continuum polarization subtraction and rotation (see text).

model, with v_0 set to $10\,\mathrm{km\,s^{-1}}$, yielded a polarization structure that was almost identical to the reference spectrum, indicating that the effect is not strongly dependent on the chosen value of the base velocity.

A further model was run in which there was no core absorption, since the width of the intrinsic absorption has approximately the same width as the effect itself. Once again, this produced no discernible change to the polarization effect, unsurprisingly since the polarization results from an optical depth effect, which is insensitive to the intrinsic absorption profile adopted. It appears that the effect itself is fairly robust and has no strong model dependence except, of course, to the adopted equatorial rotational velocity and the inclination.

Spectropolarimetric observations of the Hα emission line of ζ Puppis showed an increase in polarization magnitude through the line (HH96), which was attributed to line dilution, with the observed increase in polarization resulting from the alignment of the intrinsic and foreground vectors. Since the current model *predicts* such an increase in polarization magnitude, the observations warrant further investigation.

The observations have a small continuum polarization (~0.05 per cent), which could originate from three sources, namely the instrument, the interstellar medium, or the star itself. In order to make a comparison between the observations and the model, we must subtract this polarization, which is quite reasonable if it is interstellar or instrumental in origin since they are both in the foreground (outside the line-forming region). If the continuum polarization is intrinsic, then the wind is definitely aspherical, which will, of course, affect the line polarization morphology, rendering the comparison more ambiguous. However, since the subtraction simply corresponds to a translation in the Q–U plane, it does not affect the shape of the polarized line profile. The continuum polarization of the mean spectrum was measured over a line-free continuum bin (6760–6860 Å) and was subtracted from the observation. As the line profile structure traces a linear path in the Q–U plane, the continuum-subtracted polarization was rotated by 35° in order that all the information was in the Q Stokes parameter. The resulting polarization spectrum is plotted in comparison with the model in Fig. 10.

The similarities between the model polarized profile and the mean observation are striking. The widths of the polarization features, their maximum and minimum polarization magnitudes, and their velocity dependences are all in satisfactory quantitative agreement. In fact, the agreement is substantially better than for any of the models presented in HH96, since the polarization

structure predicted by dilution is considerably broader than that observed.

6 DISCUSSION AND CONCLUSIONS

In a series of papers, Hayes (1975, 1978, 1984) presented high-precision photopolarimetry of OB stars. He discovered variable polarization in 9 Sge (=HD 188001) (Hayes 1975), λ Cep (Hayes 1975, 1978), and κ Cas and α Cam (Hayes 1984). Typically the variability was at the 0.2–0.3 per cent level in polarization magnitude, with a time-scale on the order of a day. Hayes attributed this variability to the propagation of stellar-wind clumps. Lupie & Nordsieck (1987, hereafter LN87) published a low-resolution spectropolarimetric survey of 10 O-supergiant and O emission-line stars. It was discovered that seven of their sample showed polarization variability at the 0.2–0.4 per cent level on time-scales of days to months (although time-scales shorter than one day were not studied). They found no correlation between polarization variability with Hα variability or spectral type, and interpreted their observations in terms of electron scattering off blobs embedded in the stellar wind.

The clumped-wind model presented above shows polarization variability at the 0.1 per cent level, which is approximately three times lower than that observed by LN87. The observed levels could be obtained by increasing the density contrast of the clumps from 50 to 150 for example, but this would lead to a nine-fold increase in the emissivity of the blobs, which would imply a level of spectral variability that is at odds with that seen by ELM98. Alternatively, the size of the clumps could be increased by a factor of 3, but the emission from the clumps (essentially proportional to the emission measure $n_e^2 dV$) would correspondingly grow by a factor of 27, which would once again make the clumps too conspicuous spectrally. Richardson et al. (1996) analysed the polarization variability produced by random distributions of blobs as a function of the number of blobs, and found that the level of variability behaved differently, increasing approximately as $\sqrt{N}$. Consequently, another series of models was run, with the time-scale of blob production decreased from 2 hours to 15 minutes. It was found that the polarization variability (the standard deviation of the polarization magnitude about its mean) increased from 0.04 to 0.07 per cent, a result which is approximately consistent with the Richardson et al. model, although clearly a detailed study is required to stringently test their analytical solution.

The spiral model shows a polarization amplitude of 0.1 per cent, with two maxima per rotation period. There has been no systematic search for polarization variability of ζ Puppis on the time-scales of hours, although HH96 found a constant polarization (to within $\pm$0.02 per cent) over three consecutive nightly measurements. It appears that the current spiral model parameters produce a polarization amplitude that is larger than that predicted from the observational constraints, but a more intensive polarimetric time-series is required to resolve this issue.

Polarimetric observations by McDavid (1998) of the rapidly rotating O7.5III star 68 Cyg showed a variation with a 1.33-d period and an amplitude of 0.045 per cent. Interestingly, this is approximately half the 2.59-d rotational period inferred for the star from its equatorial rotational speed and its assumed radius. The polarization variability was found to be in phase with the equivalent width variations (with maximum polarization corresponding to maximum wind emission). Further coordinated spectroscopic and polarimetric time-series observations of this object are necessary to confirm the periodicity, while tailored spectropolarimetric models should provide a good test of rotating structures predicted by radiation-hydrodynamics models.

It should be noted that the majority of the first scatterings occur within a radial distance of $1.1R_*$, which is closer to the stellar core than even the Hα line formation region. Hydrodynamical simulations (e.g. Owocki 1994) show that radiatively driven wind instabilities are strongly damped close to the stellar surface, and that they manifest themselves only at larger wind radii. The presence of lpvs (ELM98) and polarization variability (LN87) suggests that small-scale wind structure is present very close to the wind base, and is more likely to have its origins in photospheric inhomogeneties (e.g., star spots, magnetic fields) than in line-driven instabilities.

The new line polarization models detailed in Section 5 show surprisingly good agreement with the observations of ζ Puppis. The results cast some doubt on the conclusions reached by HH96 concerning the wind geometry, since it was assumed that the line polarization morphology arose from line dilution of a polarized continuum. A further quantitative analysis of the observations is now required in order to assess the validity of the equatorial-density enhancement derived in HH96. Since the line polarization effect has an inclination dependence, it could possibly provide a method of obtaining sin i. Unfortunately, the nature of the effect is weak, and its interpretation is complicated by the presence of line-depolarization effects when the wind is even slightly non-spherical. Additionally, the low magnitude of the effect means that it is very difficult to observe, with approximately 10^6–10^7 photons per velocity bin required for a precise measurement. None the less, the power of a method that allows one to obtain a star's inclination from one measurement means that the effect merits further investigation.

The new code will be a useful tool in investigating the effects of small- and large-scale structure on the formation of emission lines in early-type stellar winds. It is apparent that a detailed investigation of the effects of wind clumping and rotation on Hα line formation is required if we are to employ Hα as a mass-loss diagnostic of stars in our Galaxy and beyond (cf. Puls et al. 1996).

ACKNOWLEDGMENTS

The author thanks Ian Howarth and Raman Prinja for useful discussions, and Joachim Puls for a swiftly produced and helpful referee's report. The computational work was performed on the UCL node of the PPARC Starlink system. John Hillier is warmly thanked for the use of his ELEC scattering code.

REFERENCES

Abbott D. C., Lucy L. B., 1985, ApJ, 288, 269
Berghöfer T. W., Baade D., Schmitt J.H.M.M., Kudritzki R., Puls J., Hillier D. J., Pauldrach A. W. A., 1996, A&A, 306, 899
Bjorkmann J. E., Cassinelli J. P., 1993, ApJ, 409, 429
Bohannan B., Abbott D. C., Voels S. A., Hummer D. G., 1986, ApJ, 308, 728
Brown J. C., 1994, Ap&SS, 221, 357
Brown J. C., McLean I. S., 1977, A&A, 57, 141
Brown J. C., Richardson L. L., Antokhin I., Robert C., Moffat A. F. J., St.-Louis N., 1995, A&A, 295, 725
Castor R. I., 1970, MNRAS, 149, 111
Chandrasekhar S., 1960, Radiative Transfer. Dover, New York
Cranmer S. R., Owocki S. P., 1996, ApJ, 462, 469

Eversberg T., Lépine S., Moffat A. F. J., 1998, ApJ, 494, 799 (ELM98)
Fox G. K., 1991, ApJ, 379, 663
Friend D. B., Abbott D. C., 1986, ApJ, 311, 701
Fullerton A. W., Massa D. L., Prinja R. K., Owocki S. P., Cranmer S. R., 1997, A&A, 327, 699
Harries T. J., 1995, PhD thesis, Univ. of London
Harries T. J., Howarth I. D., 1996, A&A, 310, 533 (HH96)
Hillier D. J., 1991, A&A, 247, 455
Hayes D. P., 1975, ApJ, 197, L55
Hayes D. P., 1978, ApJ, 219, 952
Hayes D. P., 1984, AJ, 89, 1219
Howarth I. D., Prinja R. K., 1989, ApJS, 69, 527
Howarth I. D., Prinja R. K., Massa D., 1995, ApJ, 452, L65
Howarth I. D., Siebert K. W., Hussain G. A. J., Prinja R. K., 1997, MNRAS, 284, 265
Howarth I. D., Murray J., Mills D., Berry D. S., 1998, PPARC Starlink User Note, No. 50.21
Klein R. I., Castor J. I., 1978, ApJ, 220, 902
Lépine S., Moffat A. F. J., 1999, ApJ, 514, 909
Lépine S., Moffat A. F. J., Henriksen R. N., 1996, ApJ, 466, 392
Lupie O. L., Nordsieck K. H., 1987, AJ, 92, 214 (LN87)
Maeder A., 1999, A&A, 347, 185
Massa D. et al., 1995, ApJ, 452, L53
McDavid D., 1998, in Kaper L., Fullerton A., eds, Cyclical Variability in Stellar Winds: Proceedings of the ESO Workshop. Springer, Berlin, p. 108
Moffat A. F. J., Michaud G., 1981, ApJ, 251, 133
Owocki S. P., 1994, Ap&SS, 221, 3
Owocki S. P., Cranmer S. R., Fullerton A. W., 1995, ApJ, 453, L37
Owocki S. P., Cranmer S. R., Gayley K. G., 1996, ApJ, 472, 115
Pauldrach A. W. A., Kudritzki R. P., Puls J., Butler K., Hunsinger J., 1994, A&A, 283, 525
Petrenz P., Puls J., 1996, A&A, 312, 195
Prinja R. K., Massa D., Fullerton A. W., 1995, ApJ, 452, L61
Puls J. et al., 1996, A&A, 305, 171
Reid A. H. N., Howarth I. D., 1996, A&A, 311, 616
Richards A. M. S., Cohen R. J., Yates J. A., 1997, Ap&SS, 251, 103
Richardson L. L., Brown J. C., Simmons J. F. L., 1996, A&A, 306, 519
Robert C., 1992, PhD thesis, Univ. of Montreal
Smith K. C., Howarth I. D., 1994, A&A, 290, 868
Walborn N. R., 1972, AJ, 77, 312

This paper has been typeset from a TEX/LATEX file prepared by the author.